AIAA JOURNAL
Vol. 48, No. 1, January 2010

# Control of Separation Using Spanwise Periodic Porosity

S. K. R. Patil*
*Mercury Marine, Fond du Lac, Wisconsin 54935*
and
T. Terry Ng†
*University of Toledo, Toledo, Ohio 43606*

DOI: 10.2514/1.43321

**Effects of spanwise-periodic disturbances generated by steady active ventilation on the surface of a cylinder are investigated. The wake flow is studied experimentally using flow visualization and hot-wire measurements and numerically using FLUENT™. Periodic porosity induces the formation of a series of steady counter-rotating vortex structures behind the porous patches, with or without suction being applied. A considerable closing of the wake occurs when porosity is placed on both the top and bottom surfaces, leading to a reduction in drag. The formation of spanwise vortices is suppressed, resulting in a reduction of the velocity fluctuation level and the elimination of oscillation in lift. The formation and spatial evolution of streamwise vortices is discussed.**

## Nomenclature

$C_D$ = coefficient of drag
$C_L$ = coefficient of lift
$C_m$ = suction coefficient $[\dot{m}/(\rho L D U_o)]$
$D$ = cylinder diameter being investigated, m
$d$ = hole diameter, m
$L$ = length over which suction is applied, m
$\dot{m}$ = mass flow rate, kg/s
$Re$ = Reynolds number
$r$ = radial distance from the cylinder center, m
$St$ = Strouhal number
$T$ = time for one vortex shedding cycle, s
$U$ = mean velocity, m/s
$U_o$ = freestream velocity, m/s
$u$ = rms velocity
$u_t$ = friction velocity ($\sqrt{\tau_{w/\rho}}$), m/s
$x$ = coordinate along the downstream direction, m
$y$ = coordinate along the cross-stream direction, m
$y_p$ = height of the first grid point from the cylinder wall
$y^+$ = nondimensional distance from the wall $[(\rho u_t y_p)/\mu]$
$z$ = coordinate along the spanwise direction, m
$\delta^*$ = boundary layer momentum thickness, m
$\mu$ = dynamic viscosity of air, kg/m · s
$\rho$ = density of air, kg/m$^3$
$\tau_w$ = shear stress at the wall, N/m$^2$

## I. Introduction

THE sizes and operational requirements of air vehicles, such as micro air vehicles (MAVs) and small unmanned air vehicles, are distinctly different from conventional aircraft. MAVs typically operate at Reynolds numbers in the range of 1000 to 20,000, for which the flow involves laminar separation without reattachment. For these vehicles, the main focus of a control is to delay separation (for example, by causing the flow to transition prematurely). In this study, separation control using distributed porosity is investigated at a Reynolds number typical of MAVs. Examples [1–3] of the control from several previous studies are shown in Fig. 1. A typical passive porosity system consists of a uniformly porous outer surface, a plenum, and a solid inner surface. The pressure loading on the outer surface is modified by enabling pressure redistribution between the high- and low-pressure regions through the common plenum [4–12]. Rather than uniformly distributing the control, the present concept is implemented by arranging the porosity in periodic patches across the boundary layer upstream of separation. The system can be operated using the naturally present nonuniform surface pressure or by applying suction to the plenum underneath. The control has been shown to be effective in delaying stall, increasing the maximum lift on an airfoil [1], and providing aerodynamic controls on a wing [2] and a slender body [3].

It can be envisioned that a distributed porosity will produce a three-dimensional (3-D) spanwise variation in the separation line. A visualization of the surface flow on an airfoil with the control is reproduced in Fig. 1. One prominent feature observed is the counter-rotating vortexlike structures formed in between porous patches. The main objective of the present work is to provide an understanding of the flow physics involved in this particular form of control. The study was conducted with a combination of experimental flow visualization, hot-wire measurements, and a numerical solution to the Navier–Stokes equations.

## II. Model Configuration

A baseline configuration with well-defined flow characteristics is desired in this study. In this regard, few bluff bodies have been studied as extensively as a cylinder in crossflow. There are numerous investigations on various aspects of the basic flow behaviors, and the two-volume monograph by Zdravkovich [13,14] provides a good summary of the results.

Many active and passive methods to control cylinder flow have been devised. Helical wires and strakes wound around the circumference, pairs of spheres placed along the span, streamwise eddy generators along the stagnation line, dimpled surfaces, spanwise slit, fins, circumferential grooves, and spanwise grooves are some of the passive methods studied. Some examples of active mechanical control include linear oscillation [15,16] and rotational oscillation [17,18].

Of particular interest to the present study are pneumatic techniques. Blowing or suction [19–23] modifies the mean velocity profiles in the near-wake region, which can cause alterations in the overall characteristics of associated flow instability. An investigation by Arcas and Redekopp [24] on wake control by suction/blowing concludes that the growth of absolute instability depends on both the

Presented as Paper 1410 at the 44th AIAA Aerospace Sciences Meeting and Exhibit, Reno, NV, 9–12 January 2006; received 19 January 2009; revision received 29 June 2009; accepted for publication 13 July 2009. 

*Computational Fluid Dynamics Analysis Engineer, Research and Development Department, West 6250 Pioneer Road.

†Professor, Department of Mechanical, Industrial, and Manufacturing Engineering. Senior Member AIAA.

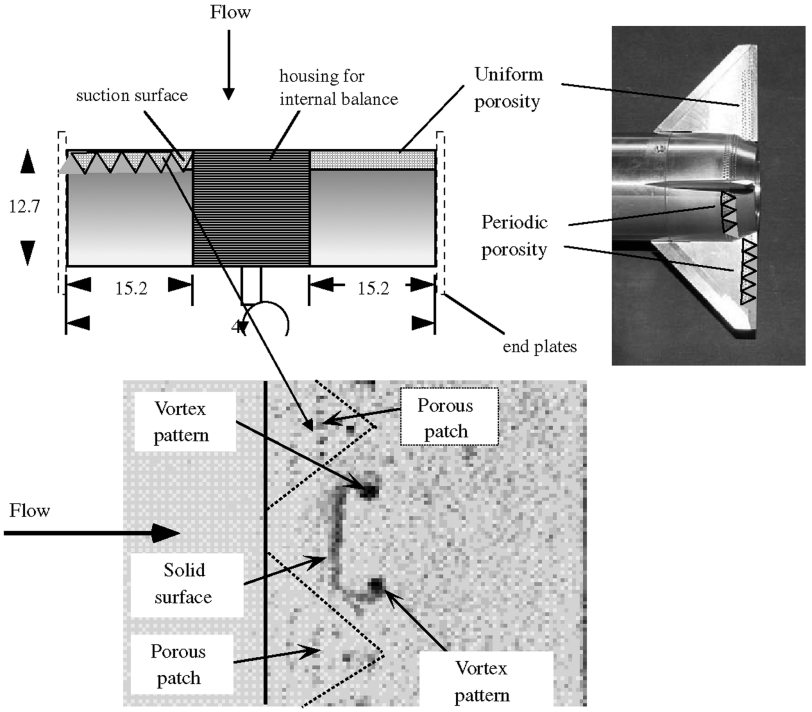


**Fig. 1 Airfoil (bottom) and projectile (top) models with periodic porosity.**

distribution and the amount of transpiration for suction but only on the amount of transpiration for blowing.

Cylinder models used in the present study are shown in Figs. 2a and 3. The diameter of the cylinder is 1.6 cm, with porosity over about 30 of its 45 cm total length. Two end plates serve as supports for placing the cylinder at the middle of the wind-tunnel test section. Each cylinder is hollow but sealed at the ends. As shown in Fig. 2a, the distributed porosity is formed by grouping 1-mm-diam holes on the surface to form triangular-shaped patches along the span. The spacing between centers of adjacent holes is 2 mm. The pattern results in a porosity of about 20% within each porosity patch. The cylinder is placed with the pointed ends of the porosity patches pointing downstream. Tubing is attached to both ends of the model to facilitate suction through a suction pump. The suction rate is monitored using a Hasting$^{TM}$ electronic mass flow meter. Two suction coefficients are used: $C_m = 0.006$ (suction 1) and $C_m = 0.01$ (suction 2).

The following cylinder models, sketched in Fig. 3, are used in the study.

1) Cylinder 1 is the baseline cylinder with a smooth solid surface.

2) Cylinder 2 is the model that contains porosity patterns at $\pm 80$ deg (measured relative to the windward stagnation line). The sawtooth patterns at the two angular positions are lined up in phase spanwise. Tests are also conducted on this model with a solid cylinder inserted internally. The outer diameter of the solid cylinder is the same as the inner diameter of the porous cylinder, which therefore prevents ventilation among the holes. With the insert, the disturbance introduced into the flow would be due only to surface roughness.

3) Cylinder 3 is the model that contains the porosity pattern at the same location as cylinder 2, but the porosity is uniform without any sawtooth patterns, such as that on cylinder 2.

## III. Methods of Study

Both experimental and computational tools are used in this study. Experiments were conducted in the Toledo low-speed wind tunnel. The tunnel is a closed-loop design, and the test section is approximately $0.9 \times 0.9$ m in cross section. The test section has a turbulence level of 0.5% or less outside of the wall boundary layers.

Smoke for offsurface flow visualization is generated by a Rosco$^{TM}$ fog generator with remote controls for smoke stream density and position. A 10 mW diode laser with remotely controlled positioning is used to generate a laser sheet with a 30 deg fan angle. The low laser power requires a chilled charge-coupled device camera to be used. Laser sheet images are captured using a relatively long exposure time, ranging from several seconds to over a minute. Surface flow visualization is conducted using an ultraviolet light source in conjunction with fluorescent dye. The velocity field is studied using a single TSI$^{TM}$ hot wire, mounted with the probe holder pointing straightforward from downstream of the cylinder.

Tests are conducted at a freestream speed of 20 m/s and a diameter Reynolds number of $19 \times 10^3$. The signal is analog filtered with a 1000 Hz low-pass frequency and sampled at a rate of 2000 Hz. Ten thousand samples are taken at each position, resulting in a sample period of 5 s and a frequency resolution of 0.2 Hz.

It is difficult to experimentally obtain some of the intricate flow details, like streamwise and spanwise vorticity, flow inside the cylinder, transpirations through individual holes, detailed vortex evolution and dissipation, and time-resolved lift and drag coefficients. Thus, simulations are used to provide these flow properties. The development of computational method is beyond the scope of our study. A well-tested and widely used computational fluid dynamics code FLUENT is used. The spatial derivatives are discretized using a second-order upwind scheme, whereas the time integration employs a fully implicit second-order backward stencil. The SIMPLE$^{TM}$ algorithm is used for pressure–velocity coupling. The system of discretized governing equations is solved using a point-implicit Gauss–Seidel relaxation along with an algebraic multigrid method to accelerate solution convergence.

## IV. Experimental Considerations

The measurement of velocity in the near wake is subjected to the general limitations of hot wire in measuring recirculating flow and resolving flow direction, as well as potential probe interference. Hot-wire measurements are thus limited to positions along the planes of symmetry of the porous patches. Even at these positions, measurements in recirculating regions are not reliable. Within these limitations, the precision of the results is ensured by several procedures. The hot wire is calibrated in situ using the wind-tunnel speed indicator. A calibration is performed before each set of measurements. Positioning of the probe is provided by a stepper motor driven 3-D traverse with a spatial resolution of $10^{-3}$ mm. The

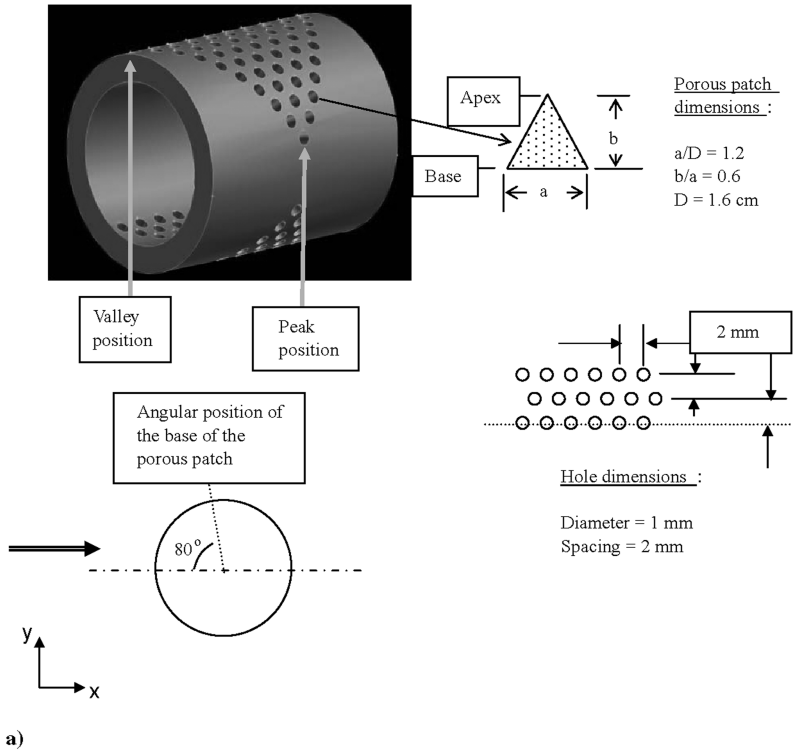


a)

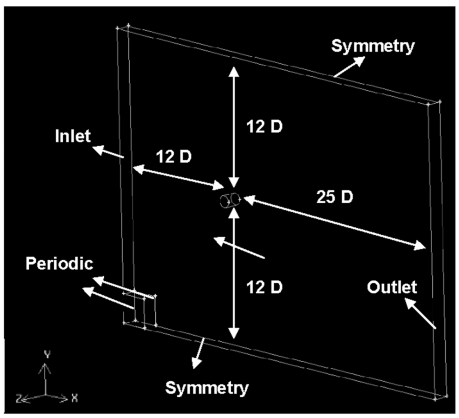


b)

**Fig. 2 Periodic porosity and computational domain configuration used in the present study: a) dimensions of the periodic porosity used on cylinder 2; and b) computational domain size used for the numerical study.**

main uncertainty in positioning is in determining the initial hot-wire position relative to the cylinder model. To minimize this uncertainty, a reference position is obtained using a dummy hot-wire probe to physically contact a reference point at the 180 deg mark on the cylinder. The dummy probe is then replaced by an active probe of identical dimensions.

Wake surveys are conducted for each model. For $x/D$, from 0 to 1.5 measurements are taken with 1 mm vertical position resolution over $y = \pm 40$ mm at several $x$ positions. The measurements are then repeated using a grid with a 5 mm resolution for $y = 20$ to 100 mm at the same streamwise positions. A number of common measurement points will result from these two grids. The standard deviation among these points is calculated, and a value of about 0.6% of freestream speed is obtained. The results indicate a satisfactory repeatability and an acceptable overall uncertainty. For $x/D$, from 2.0 to 6.0 measurements are taken with a 2 mm position resolution over $y = \pm 80$ mm.

## V. Computational Considerations

In addition to grid and computational domain sizes, one of the main considerations of the computational study is the state of the boundary layer. At the subcritical $Re = 19,000$ for crossflow over a smooth cylinder, the boundary layer is laminar and the wake is turbulent. With spatially periodic suction along the span, however, the state of the flow remains to be established. In the case of natural transpiration, both blowing and suction occur over a porous patch. Blowing from periodic holes can be an effective means of promoting transition. Low-rate suction, on the other hand, removes the low momentum fluid from the wall and can make the velocity profiles less prone to transition to a turbulent state. Above a critical value of suction flux, however, the phenomenon of oversuction can occur. Macmanus and Eaton [25] report critical suction velocities for different ratios of $d/\delta^*$, at which the flow transitions to turbulence owing to oversuction. The present simulation on the smooth cylinder results in a $d/\delta^*$ of 2.0, which yields a critical suction velocity of $0.2U_0$. Simulations on the porous cases show that the suction velocity through the holes varies but is greater than $0.2U_0$ for the suction rates tested, which implies possible suction-induced transition to turbulence. The experiments by Macmanus and Eaton [25] are on a flat plate with a zero-pressure gradient. For flow over a cylinder with a strong adverse pressure gradient, this value is expected to be even lower, leading to an early transition. Other factors

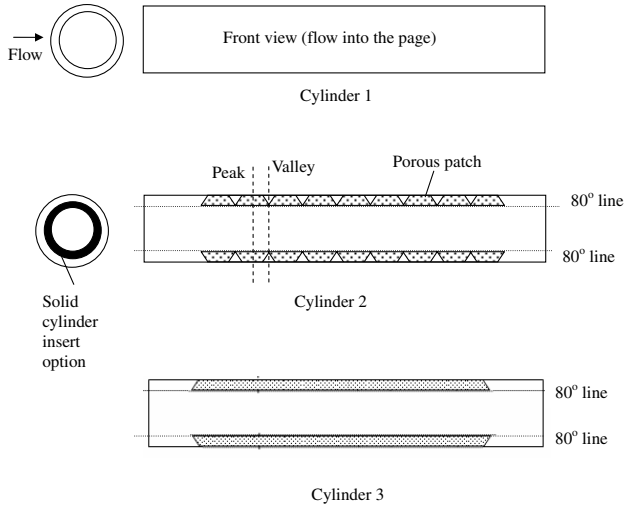


**Fig. 3 Cylinder models studied. Cylinder 1 is a smooth cylinder with no porosity. Cylinder 2 has a spanwise-periodic porosity with a hollow plenum for crosstalk between the porosity holes. This cylinder also has an option for a solid cylinder insert, which would close the plenum and leave the surface with the roughness of the holes. Cylinder 3 has uniform porosity. Porosity patches start at 80 deg from the stagnation point for both cylinders 2 and 3. This corresponds to the separation line location for laminar crossflow over a cylinder.**

favoring transition in the present case include nonuniform distribution of suction [26], triggering of a secondary instability by free stream turbulence [27], and interaction between local disturbances and Tollmien–Schlichting waves [28].

The computational determination of the exact location or Reynolds number for transition, critical suction rate, or the effect of freestream turbulence will be extremely difficult in such a multiple flow instability scenario. Although the actual flow upstream of porous patches is laminar and the wake is turbulent, the numerical model considers the whole flow either to be turbulent or laminar due to the inability of FLUENT to predict transition the point and, accordingly, switch from laminar to turbulent modeling. As such, the inability of FLUENT to model transition can be a major limitation to our numerical study.

When the flow is assumed to be turbulent, the boundary layer is modeled using Reynolds averaged Navier–Stokes (RANS) equations, with closure equations [29,30] for Reynolds stresses. The use of RANS methods instead of large eddy simulations (LES) or direct numerical simulations (DNS) for predicting unsteady flows that contain vigorously organized and periodic components may lead to underresolved and dissipative results. For flows in which the time periodic unsteadiness is the result of an inherent instability, the instability mechanism has to be strong, and the turbulence model should be of high accuracy to ensure that the instability is not damped out altogether. For example, vortex shedding in the wake of a cylinder due to absolute instability is a strong instability mechanism that has been resolved with RANS models with a good comparison to the experimental results. Unsteady flows with external forcing, as is our case, are less challenging for RANS schemes, as they generally capture the first-order response of the flow to the forcing.

**Table 1 Different grid configurations used on cylinder 2 for studying grid dependency of the solution. BL is the number of orthogonal nodes in the boundary layer; cylinder and hole denote the number of nodes around the perimeter of the cylinder and the suction holes, respectively; $x$, $y$, and $z$ denote the number of nodes in the respective directions; and total cells denotes the final size of the mesh**

| | BL | Cylinder | Hole | $Nx$ | $Ny$ | $Nz$ | Total cells |
|---|---|---|---|---|---|---|---|
| Grid 1 | 10 | 90 | 10 | 80 | 60 | 30 | 1.2 million |
| Grid 2 | 15 | 180 | 15 | 120 | 80 | 40 | 1.9 million |
| Grid 3 | 25 | 180 | 30 | 200 | 120 | 60 | 4.2 million |
| Grid 4 | 30 | 240 | 40 | 240 | 160 | 100 | 7.4 million |

RANS models have been used previously [31–33] to predict active flow control with good fidelity. Even with a rapidly fluctuating external perturbation, RANS models give satisfactory results [34]. Also, a bench mark study [35] concluded that steady suction/blowing modeled by RANS gives better comparable results with experiments than unsteady suction/blowing investigated with RANS. Bluff body flows predicted [36,37] using unsteady RANS (URANS) yield satisfactory results when compared with LES and experiments. A recent study [38], which used the same code as in the present work, shows that $3D$ URANS on a surface-mounted cube yields agreeable results with experimental data when the flow is not statistically stationary. Merigaud [39] suggests that to reliably calculate the turbulent boundary layer subjected to suction, a relatively sophisticated turbulence model [such as the Reynolds stress models (RSMs)] should be used for closure. Djenidi and Antonia [40] show that second moment closures used to calculate the steady turbulent boundary layer, subjected to concentrated wall suction, reproduce the effect of suction on skin friction coefficient mean velocity and Reynolds stresses observed in measurements and in DNS data. As RSM offers better reliability than algebraic or zero-equation or two-equation models, the RSM turbulence model is used in the present case.

With the exception of some preliminary computations, a single periodic part of the cylinder is used in the computational domain, as shown in Fig. 2b. The spanwise boundaries and transverse boundaries are set to a periodic boundary condition and a symmetry boundary condition, respectively. After grid convergence studies on a $2D$ cylinder flow with various streamwise and transverse stream computational domain lengths, the inlet is placed $12D$ upstream, the outlet at $25D$ downstream, and the transverse symmetry planes at $\pm 12D$.

A grid dependence study is performed on cylinder 2 using the four different mesh configurations given in Table 1. Computational nodes along all three directions and around the perimeter of the cylinder and suction holes are increased gradually to create four different meshes. The velocity profiles (in Fig. 4, at a cross-stream plane of $x/D = 0.75$) on these four mesh configurations show that grid 1 is too coarse to capture the proper shear layer development. The solution becomes more consistent when the mesh size is increased from grid 2 to grid 3, and there is no change in the solution when the mesh size is increased from grid 3 to grid 4 (see Fig. 4). Based on these results, grid 3 with 4.2 million cells is selected for all the simulations reported. This computational domain and mesh size is comparable with the investigation of streamwise vorticity in the wake of a circular cylinder by Kim [41], the results of which agreed well with experiments. The near-wall mesh resolution is such that the distance from the cylinder surface at the wall-adjacent cells is $5 \times 10^{-4} D$. This value of the physical wall distance translates to $y^+$ values well below 1.0.

## VI. Initial Experimental Results

Experiments are performed on the porous cylinder models with and without external suction. The suction case simulates a control mode in which all the surface holes are ventilated to a suction source, resulting in a finite net mass flow. The no-suction mode simulates a control based on natural ventilation within a suction patch and also between patches. In this case, both suction and blowing occur over a porous patch, resulting in a zero net mass flow.

### A. Flow Visualization Results

Some wind-tunnel and water-tunnel visualization results of the prototype cylinders have been reported by Ng [42]. Examples of the wind-tunnel flow visualization from the study are shown in Fig. 5. The surface pattern shows the formation of a series of counter-rotating structures behind the porous patches. The laser sheet results, such as Fig. 5b, reveal several flow features (not all shown here).

1) There is a considerable closing of the wake of cylinder 2 due to porosity.

2) Two distinct flow regions, labeled 1 and 2, exist in the wake of the porous cylinder.

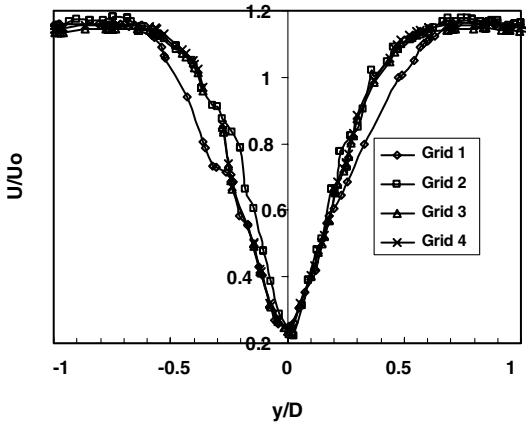


**Fig. 4 Time-averaged velocity profile for cylinder 2 at an $x/D = 0.75$ cross-stream plane obtained using four different mesh configurations.**

3) Flows along the peak and valley positions of the suction pattern show a significant spanwise variation in flow region 1.

These photos represent integrated images over a relatively long period of time. As seen by the naked eye, the structure in region 1 is relatively steady, whereas region 2 exhibits a significant unsteadiness. The lack of clarity in the present photos, however, precludes a more detailed analysis of the structure. Nevertheless, the laser sheet and the surface flow results together suggest the existence of a relatively steady 3-D recirculation region immediately behind the porous patches, followed by an unsteady wake.

### B. General Impacts of Porosity on the Wake Velocity Field

The degree of modification to the near wake, as caused by periodic porosity, is interrogated using a hot wire at the peak and valley positions (as defined in Fig. 2) for $0.5 \leq x/D \leq 0.69$, approximately covering wake region 1 in Fig. 5. Differences between mean velocity profiles (Fig. 6) at the peak and valley positions become relatively small downstream of $x/D = 0.69$. Hence, only results at the peak position will be reported for $x/D > 0.69$, even though measurements are always taken at both peak and valley positions.

Figure 7 compares mean velocity profiles of cylinder 1 and cylinder 2 at $x/D = 0.75$. The smooth cylinder 1 produces the typical shear layer and wake profiles. The wake behind the periodic porous cylinder is narrower, and the maximum mean velocities at the shear layer are lower characteristics that suggest a delayed separation. The corresponding rms profiles in Fig. 7b show two main features of the periodic porous cylinder in relation to the smooth one. First, a reduction in rms occurs across the entire $y/D$ range. Second, there is an approximate reduction of two-thirds in the peak rms level.

### C. Role of Surface Roughness

Porosity can have two effects on the flow. First, the holes can act as surface roughness that trips the boundary layer. Second, natural ventilation among the holes can produce local suction and blowing. The relative importance of these effects is demonstrated in Fig. 7. The figures compare velocity profiles of cylinder 1 and cylinder 2 with natural transpiration, and cylinder 2 with surface roughness only. Although results at several streamwise positions are obtained, only $x/D = 0.75$ is shown, because all the results lead to the same conclusion that the roughness has a relatively very minor effect on the flow character.

## VII. Simulation Results

Because of potential issues, such as grid resolution, computational domain size, boundary layer modeling, and (in particular) the inability to accurately simulate the transition process, the initial verification of the computation results will be based on the ability to reproduce the experimentally observed global features of the wake.

### A. Smooth Cylinder 1: Laminar Case

The computational result of the smooth cylinder shows the typical shear layer and wake development. The separation point is at 80 deg, which is consistent with the typical value for laminar flow. Vortex shedding at a frequency consistent with experimental results is observed, and the wake spreads in the streamwise direction as expected.

### B. Periodic Porosity Cylinder 2, Natural Transpiration: Laminar Case

*1. Steady Solution*

The effect of natural transpiration on the near-surface flow is revealed in Fig. 8. Three porous patches were included in this preliminary computation to obtain the interaction between the vortices generated. As shown by the streamlines, the flow possesses

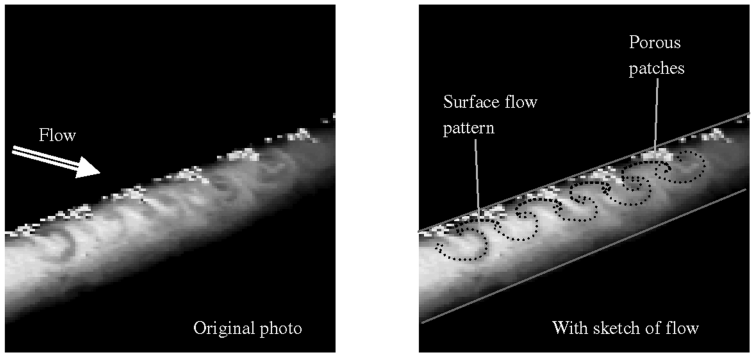


**a) Fluorescence oil on the surface of the cylinder 2 with suction level 1**

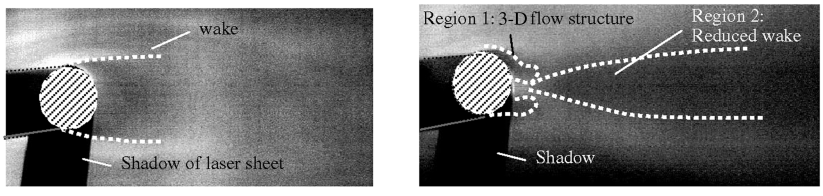


**b) Laser sheet - smooth cylinder** **c) laser sheet - model 2 at the peak position**

**Fig. 5 Visualization of the cylinder flowfields.**

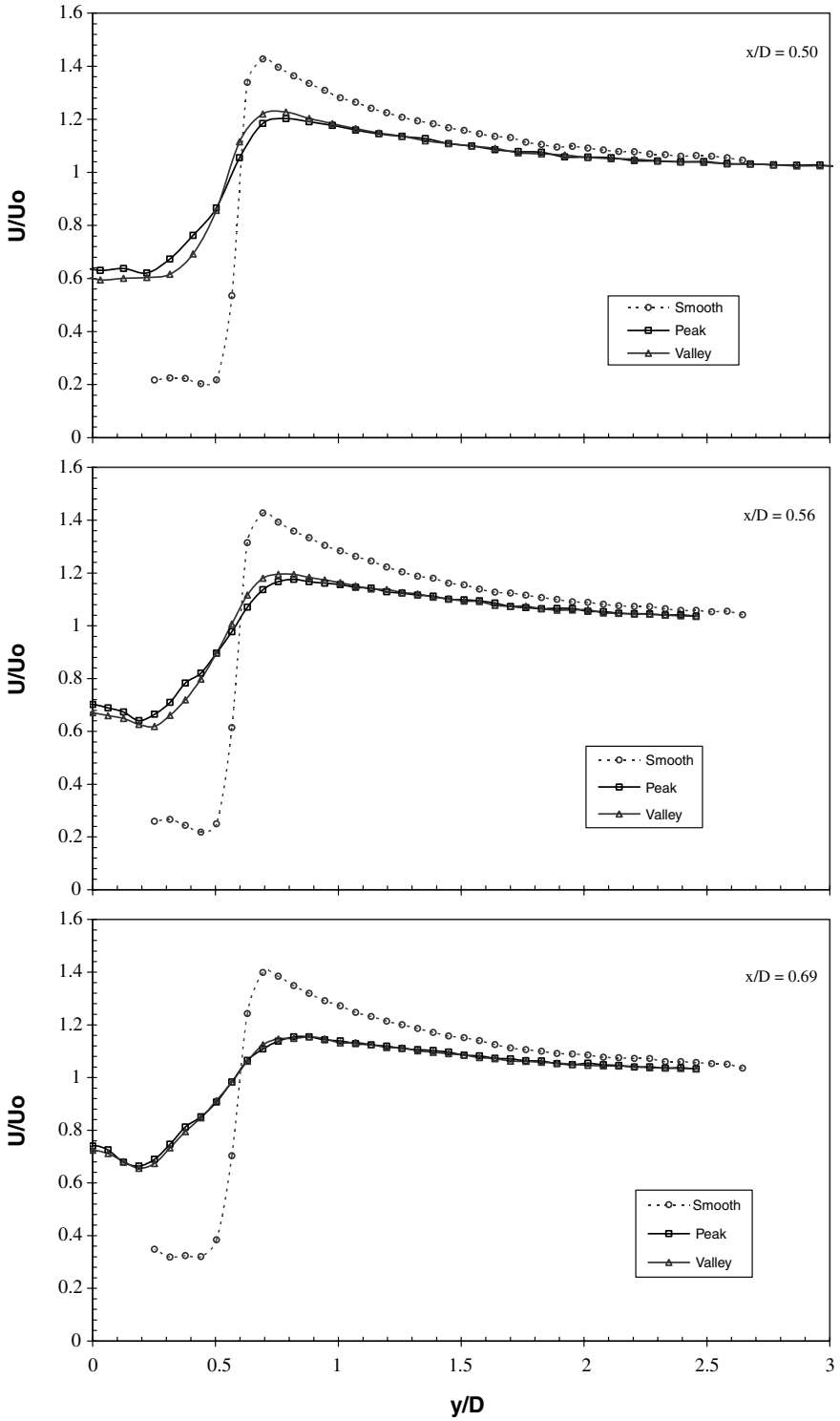


**Fig. 6 Measured near-field mean velocity profiles for cylinder 1 (smooth) and cylinder 2 (periodic porosity).**

strong 3-D features compared with the flow over a smooth cylinder. The numerical results are also qualitatively validated by experiments for which, in all cases, a counter-rotating streamwise vortex pair is formed over each of the porous patches. The computational surface flow visualization on cylinder 2 shows the formation of counter-rotating vortex patterns. This is consistent with the experimental results shown in Fig. 5. Streamwise vortices in the flowfield for cylinder 2 are captured by the steady-state solver, an example of which is shown in Figs. 8 and 9. Several observations can be made on the steady simulation.

1. Periodic surface porosity produces different separation patterns and wake flow for which the structure is highly 3-D.

2. Counter-rotating streamwise vortex patterns are observed in the wake. Because of their opposite rotation directions, the vortices persist without mixing. This suggests use of a periodic boundary condition on the surfaces, shown in Fig. 2b.

3. The results show closing of the wake of the cylinder in the presence of periodic surface porosity.

### 2. *Time-Accurate Laminar Solution*

In situations, such as the present case, that involve two competing instabilities, the eventual flow state will depend on the initial perturbation amplitudes and amplification rates. In the present case,

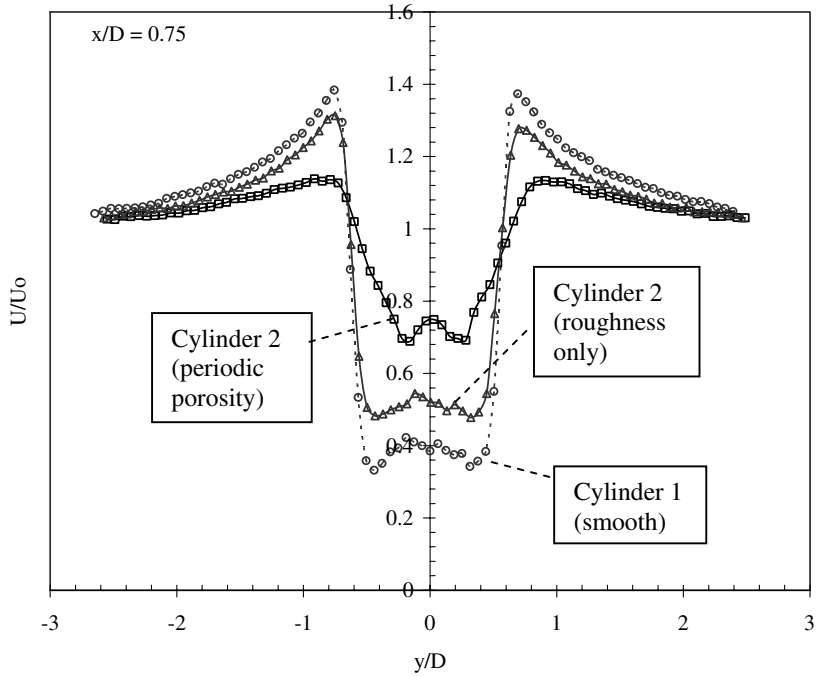


a)

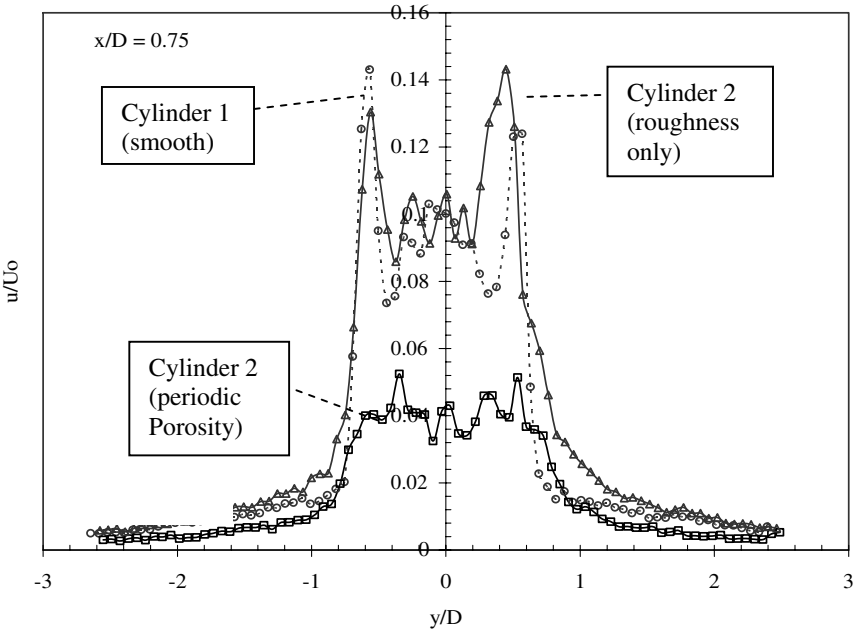


b)

**Fig. 7 Comparison of a) mean velocity profiles and b) rms velocity profiles with ventilation (cylinder 2 with periodic porosity) and without ventilation (cylinder 2 with roughness) at peak position.**

there are two types of instabilities. The first is the global instability that manifests in the vortex street [Kelvin–Helmholtz (K–H) instability]. The second is the convective instability that results in a streamwise vorticity concentration. In the steady-state simulations, the time-varying global instability is artificially removed, leaving only the convective instability. In the absence of imposed perturbation/control, the K–H instability will dominate due to its naturally higher rate of amplification. In the presence of a sufficiently large spanwise periodical perturbation, however, the convective instability can dominate. Therefore, results of transient laminar simulations with the spanwise-periodic porosity show streamwise vortex formation, similar to that of steady-state simulations for first few time steps. After the initial time steps, however, the flow reverts back to the usual laminar crossflow over a cylinder with spanwise vorticity concentration and a separation at 80 deg from the stagnation point. That is, the transient laminar solution does not show sustained streamwise vortices. Further investigation into the flow showed that the formation of streamwise vortices ceases as soon as the separated shear layers start to oscillate. This occurs when the oscillation of shear layers feeds back to the cylinder to cause an oscillation of the separation positions. When the transient separation location moves upstream of the suction patches, the pressure over the suction patches becomes almost uniform, and transpiration among holes is reduced. This removes the initial perturbation needed for the convective instability. The effect is amplified by the occasional suction only on the top patches of the holes and blowing only from the bottom

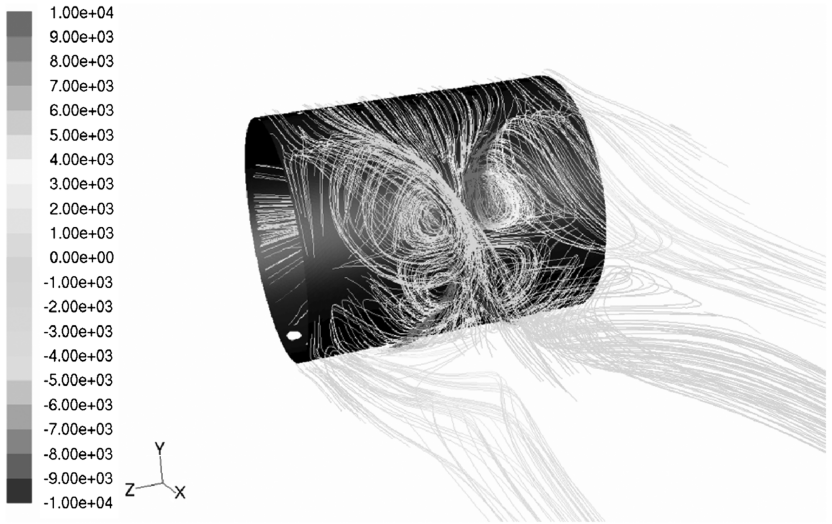


**Fig. 8 Streamlines colored by streamwise vorticity ($1/s$) for flow on cylinder 2 with natural transpiration. Flow is assumed to be laminar in this steady-state solution.**

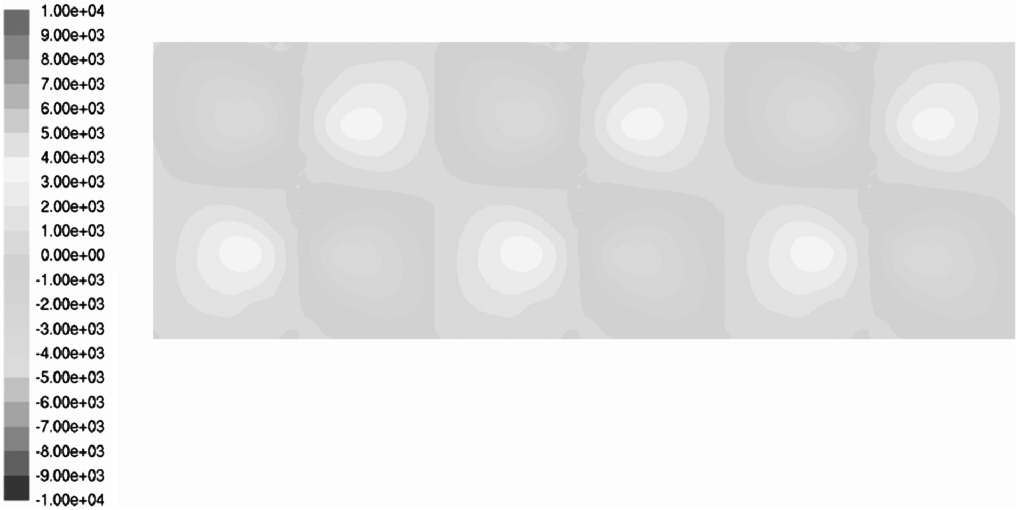


**Fig. 9 Computed streamwise vorticity ($1/s$) at $x = 1.5D$ for cylinder 2 with natural transpiration. Flow is assumed to be laminar in this steady-state solution.**

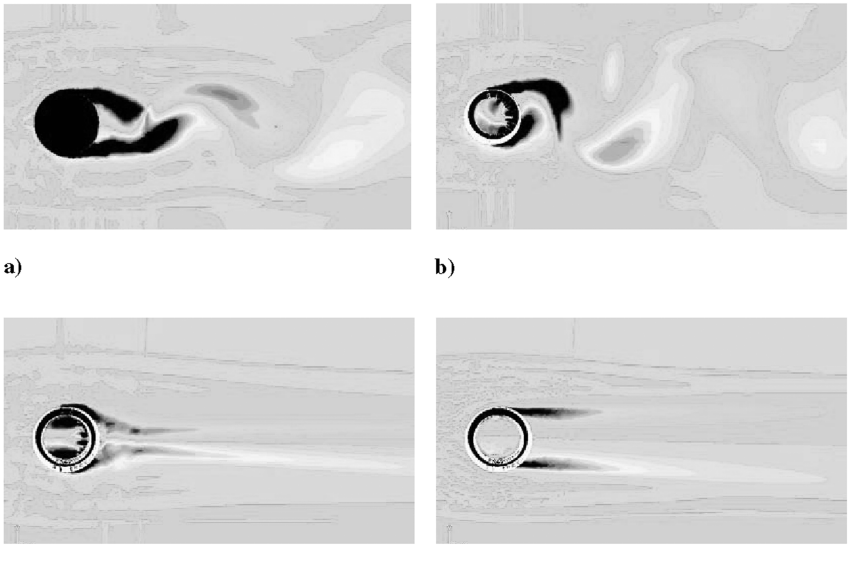


**Fig. 10 Instantaneous spanwise vorticity for a) a baseline case, b) a uniform spanwise porosity, and c) peak and d) valley positions for periodic spanwise porosity.**

patches of the holes for half of the vortex shedding cycle, and vice versa for the other half. Once the imposed perturbation is reduced, the K–H instability takes over, resulting in the dominance of spanwise vortices. It may be conjectured that if transition has taken place (as supposed in the experiments), the separation location will be farther downstream and stay over the suction patches. Thus, initial perturbation for the convective instability is therefore maintained, and streamwise vortex formation sustained.

As a final test, the steady-state simulations are allowed to run for more than 5000 iterations. At that point, streamwise vortices start to break in symmetry and finally disappear, giving way to the spanwise vortices. This alludes to the reasoning that the numerical error accumulated during these initial iterations could have acted like a perturbation to the flow consisting of streamwise vortices and led to formation and domination of K–H instability.

### C. Periodic Porosity Cylinder 2, Natural Transpiration: Turbulent Case

Computations are conducted to determine whether, with zero net mass transpiration, a turbulent velocity profile can sustain the streamwise vortices. Overall, the flow behaves similarly to the laminar case. Initially, streamwise vortices are formed, but as the flow progresses, spanwise vortices form, and soon the shear layers oscillate, resulting in the termination of the streamwise vortices. In this case, and as opposed to the laminar situation, it is conjectured that the turbulent separation point is too far down of the suction patches, disabling the periodic porosity to induce any convective instability for streamwise vortex formation.

In conclusion, the computations did not successfully simulate the experimental observations of the natural transpiration case, regardless of the assumed state of the boundary layer. Although many potential reasons existed, we suspected the main reason could be the low perturbation amplification rates provided by the natural transpiration that demanded a fine mesh and a non-RANS solverlike direct numerical simulation or at least an LES. The inability to accurately simulate the transition process over the porous patches could have also exacerbated the problem in resolving the instability seen in the test.

### D. Nonzero Net Transpiration Through Suction: Laminar Case

As natural pressure differences are unable to provide sufficiently strong perturbations in simulation, suction is applied to the end faces

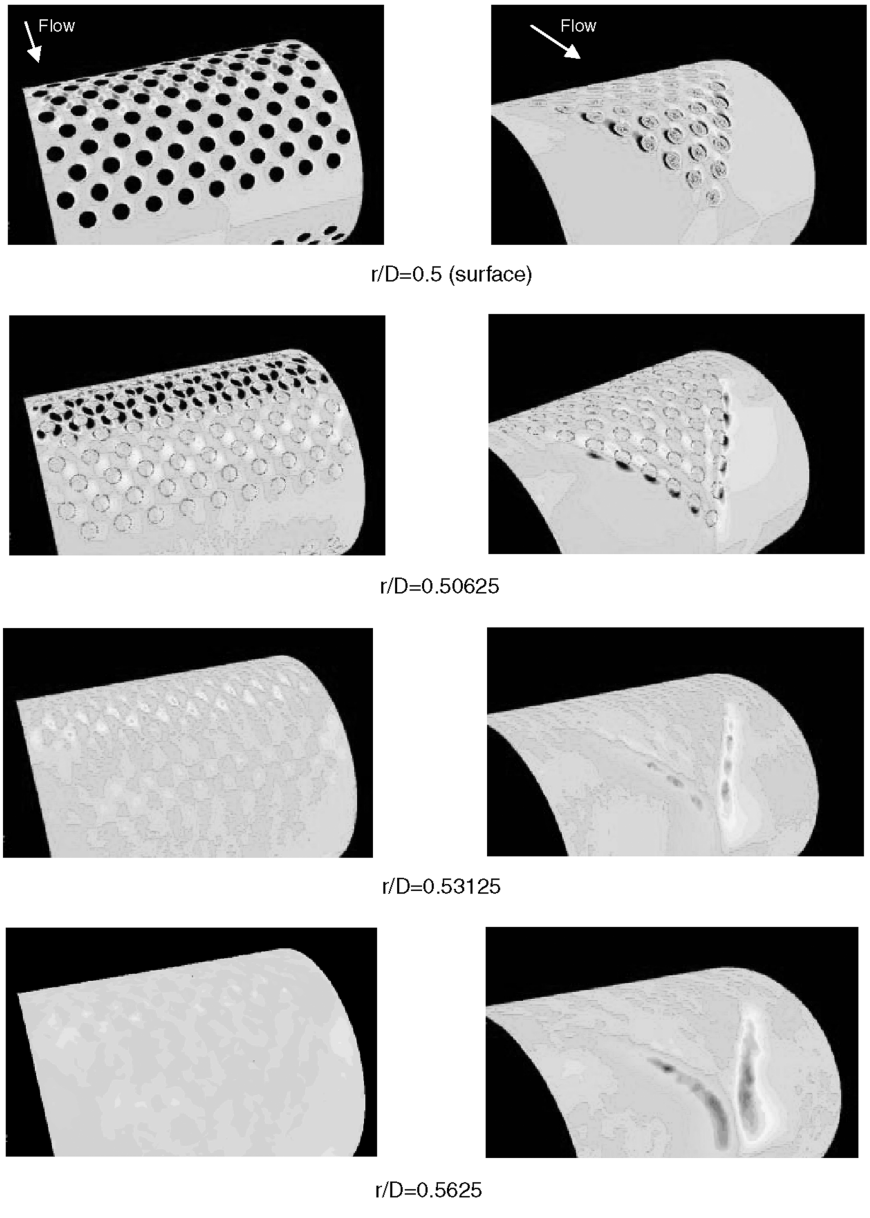


**Fig. 11 Evolution of streamwise vorticity at various radial distances *r* from the cylinder centerline for a) uniform spanwise porosity (cylinder 3) and b) periodic spanwise porosity (cylinder 2).**

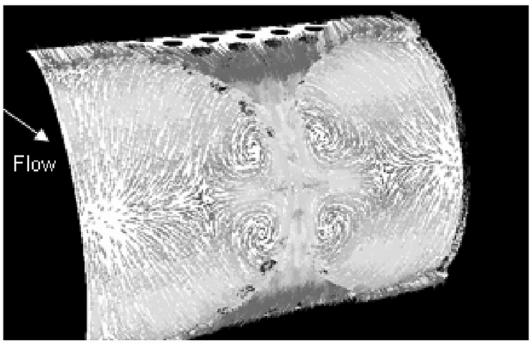


**Fig. 12 URANS simulation of the surface flow of cylinder 2, as indicated by velocity vectors.**

of cylinder 2 at sufficient suction rates to eliminate blowing through any of the surface holes. Thus, the technique of imparting 3*D* perturbations is now active, with energy being spent for suction of air through porous patches.

The suction condition is applied to cylinder model 2, and a transient laminar flow analysis is performed. The streamwise vorticity again cannot be sustained beyond the first few vortex shedding cycles. Suction is increased two, four, six, eight, and 10 times the experimental value, and none of the numerical experiments retains the streamwise vortices in the long term. For low suction rates, the spanwise structure of the spanwise vortices is not affected much. For high suction rates, the formation of spanwise vortices is suppressed, but streamwise vortices are not retained. Based on the experimental results, it is decided that some essential flow physics are not being resolved or represented in the governing equations, again, with the inability to model transition being one of the possible causes.

### E. Nonzero Net Transpiration Through Suction: Turbulent Case

Of all the computational cases, this is the only one that successfully captures sustained streamwise vorticity formation in the flow. Because FLUENT 6.2 can only simulate flows that are either completely laminar or turbulent, this is obviously not the same as the experimental situation, which is laminar until the separation point and the free shear layers are turbulent. Nevertheless, the flow characteristics obtained from the simulation and experiments do share a good degree of similarity, and therefore will be compared in the following discussions. A simulation with spanwise uniform porosity (as shown in Fig. 3) and steady suction is conducted for a suction coefficient of 0.01, which is higher than the suction coefficient of 0.006 applied to cylinder 2 in tests and simulation.

## VIII. Fluid Mechanism of the Control

The global effects of different controls on the flowfield are demonstrated in Fig. 10 using the instantaneous spanwise vorticity contours obtained through simulations. For a smooth cylinder, the vorticity in the shear layer is concentrated in the spanwise direction (Fig. 10a). The flowfield for the uniform porosity case (Fig. 10b) is similar to the baseline case. Thus, even with a higher suction coefficient than the periodic porosity case, uniform porosity does not prevent spanwise vortex formation. This suggests that suppression of K–H instability is not due to suction but due to a convective instability. The periodic porosity case results in Figs. 10c and 10d show no spanwise vortex formation in the shear layers. Additionally,

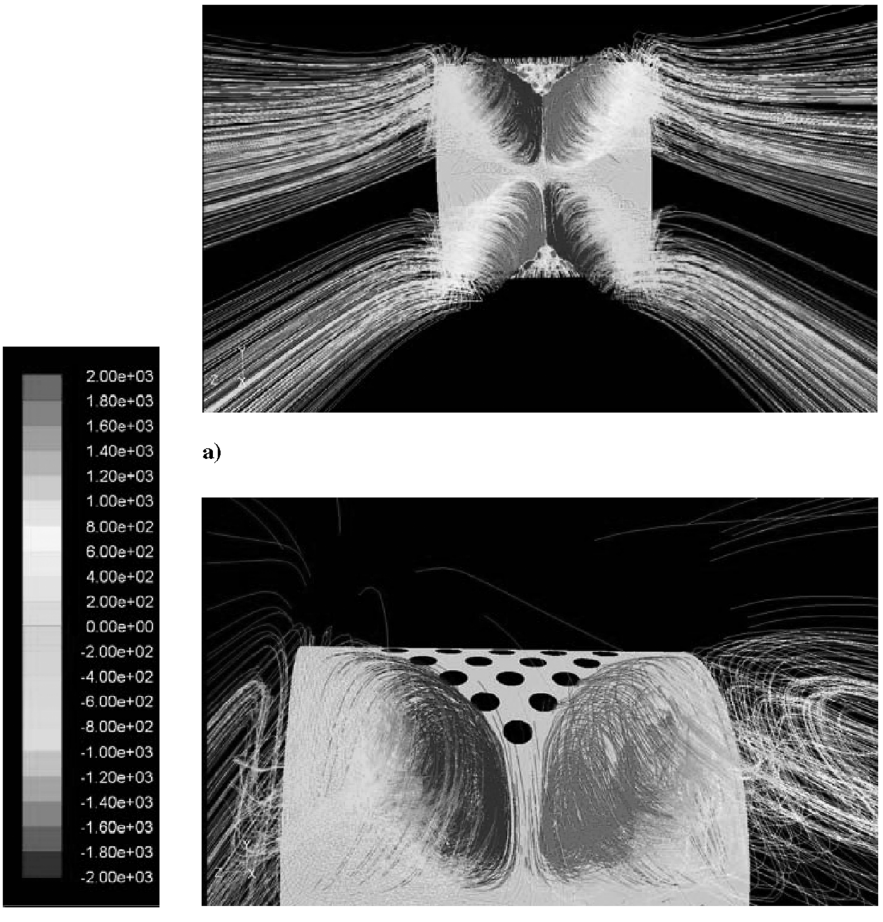


**Fig. 13 Path lines of flow over cylinder model 2, colored by streamwise vorticity (rad/s): a) path lines in near and far wake combined and b) path lines in near wake. Upstream view, looking from downstream in the wake.**

there is a difference in spanwise vorticity at the peak (Fig. 10c) and valley (Fig. 10d) positions.

### A. Vorticity Concentration Near the Surface

The simulated spatial growth of streamwise vorticity for two porous cylinder models is shown in Fig. 11. From now onward, vorticity will refer to streamwise vorticity unless specified otherwise. Localized vorticity with an opposite sense of rotation is developed at the wall and in the boundary layer for cylinders with porosity. For all cylinders, the near-wall streamwise vorticity is generated by suction through the holes. Farther away from the surface, the vorticity is less localized near each hole as the vorticity merges with that at the adjacent holes and diffuses into the boundary layer. From $r/D = 0.50625$ to $0.53125$, the vorticity over most of the porous patch is one order of magnitude less compared with at the wall and is more uniform. For the uniform porosity case, shown in Fig. 11a, the vorticity is completely dissipated at $r/D = 0.5625$. For the cylinder with periodic porosity, however, the vorticity at the edges of each patch is sustained and amplified, as can be seen in Fig. 11b. At $r/D = 0.5625$, only the vorticity at the edges of the porous patches is seen, whereas the local vorticity generated by the holes in the center portion of the porous patch is dissipated.

### B. Formation of Near-Surface Counter-Rotating Vortex Motion

Figure 12 shows the flow pattern on the cylinder 2 surface. The result reveals that the line of separation is 3-D, with a pattern following the outer edges of the porous patches. A counter-rotating streamwise vortex pattern is observed on the surface of the cylinder, downstream of the porous patch. In contrast to the transient laminar simulation, the pattern is observed at all instances of time on the surface of the cylinder and is more defined.

### C. Effect of Periodic Porosity on the Wake Shear Layers

Figure 13 shows the stationary, spatially periodic, streamwise vortices and vorticity in the shear layer. The path lines reveal the formation of the symmetric counter-rotating streamwise vortex pair: one at the top porous patch and another at the bottom porous patch. The vorticity dissipates in a downstream direction and is negligible after a distance of three diameters downstream. This configuration of equal and opposite vorticity adjacent to each other results in a stable vortex configuration. Streamwise vortices have been previously observed [43], in which they were generated by helically winding a wire over a circular cylinder and in crossflow over a sinusoidal cylinder [44,45]. In these cases, however, the streamwise vortices were not stationary and did not completely subdue the formation of spanwise vortices in the near wake.

The growth of the vorticity generated in the boundary layer into steady large streamwise vortices is similar to that observed experimentally by Lasheras et al. [46]. In their experiment on a plane free shear layer, they demonstrate the mechanism of the re-distribution of spanwise vorticity into axial vorticity. According to their theory, a small deformation of the axis of primary spanwise vorticity is stretched in the streamwise direction due to positive strain, producing a pair of counter-rotating vortices. Under their influence, the vortex lines are further lifted upward at the sides of the evolving longitudinal vortices. The vertical shear and/or strain then orient the vortex axis in the axial direction, where the positive strain will continue to stretch the pair of vortices. In the present case, the small deformation to spanwise vorticity near the separation point is provided by suction through groups of holes arranged in periodic patches along the span of the cylinder. One key difference from the mechanism described by Lasheras et al. [46] is that in the periodic suction case, no spanwise vortices are found to be needed for the streamwise vortices to grow. Based on linear stability analysis, Pierrehumber and Widnall [47] also numerically explain the redistribution of primary spanwise vorticity into the direction of the strain field (axial) via a mechanism called translative instability. They conclude that translative instability is broadband in nature and at short wavelengths has growth rates comparable with K–H instability.

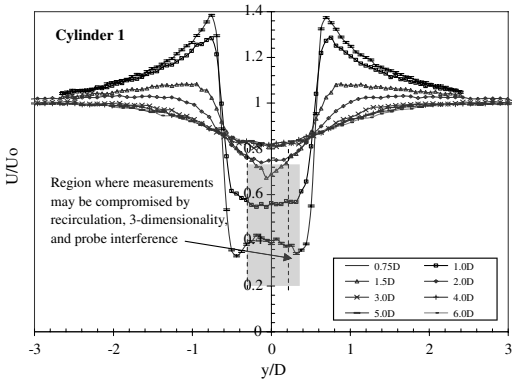


a) Experiment

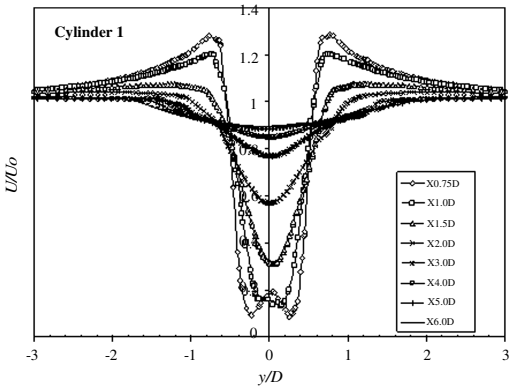


b) Computation

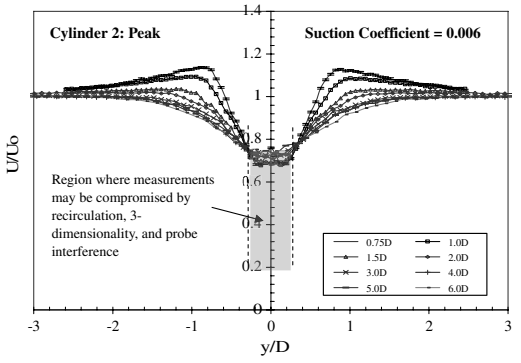


c) Experiment

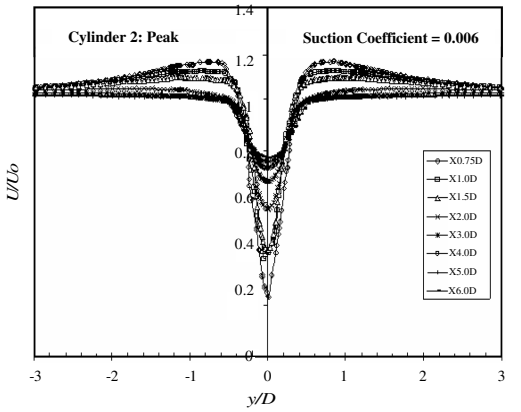


d) Computation

**Fig. 14 Comparison of test and computations: time-averaged laminar velocity profiles for cylinder 1 from a) test and b) computations for peak position at various downstream locations, and time-averaged velocity profiles for cylinder 2 at various downstream locations in the wake at peak position from c) test and d) URANS computations.**

The present study suggests, with a sufficiently large initial perturbation, that translative instability can become the dominate instability and suppress the K–H instability.

The mean velocity profiles obtained from experiments and turbulent simulation are shown in Fig. 14. For the porous cases, measured velocities in the near wake are compromised by the limitations of hot wire in measuring recirculatory flows and resolving flow direction, as well as potential probe interference. Also, due to the inability of the present numerical method to simulate transition and accurately determine the separation location on the cylinder, the numerical results may vary from the hot-wire measurements. Nevertheless, the spatial evolution of the wake predicted by simulation agrees reasonably well with results from experiments, except in the near-wake region. The agreements include non-recirculating zone shear layer development of laminar flow over cylinder 1 (Figs. 14a and 14b) and the narrowing of the wake and reduction of the maximum mean velocity in the shear layer for cylinder 2 (Figs. 14c and 14d). Figure 15 shows the rms velocity profiles obtained using hot wire at different cross-stream planes. Periodic porosity on the cylinder considerably reduces the wake fluctuation when compared with the smooth cylinder.

### D. Effects on Periodic Lift and Drag

Figure 16 shows the time-dependent lift and drag coefficients for simulated turbulent flow past cylinder models 1 and 2 at $Re = 19,000$. Although the boundary layer is laminar at this $Re$ on cylinder 1, a turbulent simulation is performed to compare with the probable turbulent flow generated by oversuction on cylinder 2. The computational time step is selected to be $T/40$, where $T$ is the time

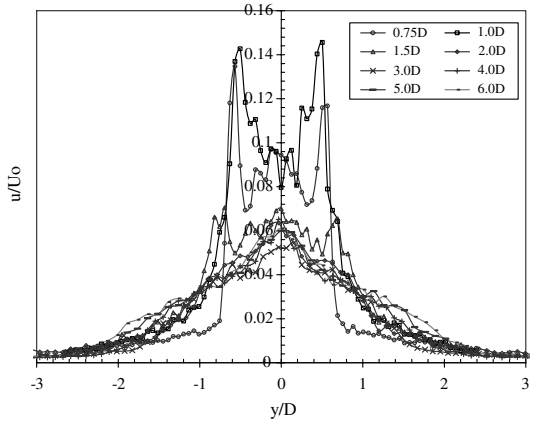


**a) Cylinder 1**

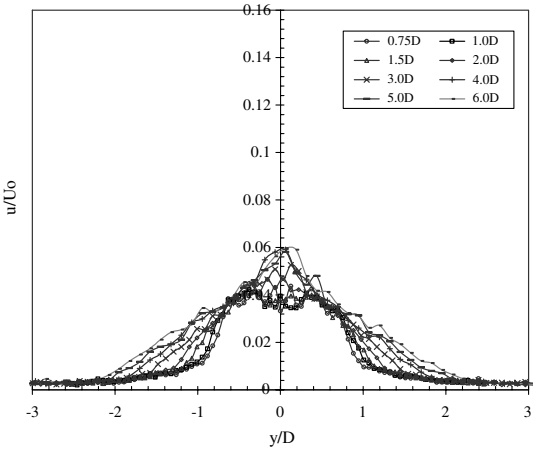


**b) Cylinder 2**

**Fig. 15 Comparison of the rms velocity profiles obtained using hot wire at different streamwise positions: a) smooth cylinder 1 and b) periodic porosity cylinder 2.**

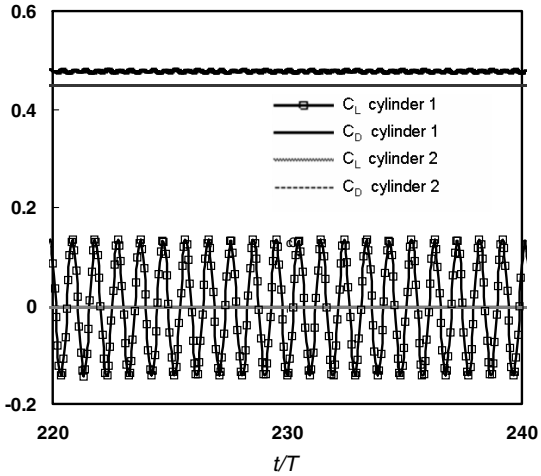


**Fig. 16 Transient lift and drag coefficients for cylinder 1 and cylinder 2 with suction, obtained using URANS for turbulent flow.**

for one vortex shedding cycle, calculated assuming a Strouhal number of 0.2. The solution is obtained for 300 periodic vortex shedding cycles to remove any initial transients present in the solution and obtain a well-converged statistically periodic solution. The lift coefficient fluctuation amplitude and mean drag coefficient obtained are 0.16 and 0.47, respectively, for cylinder 1, which are consistent with those measured [13] in a turbulent regime for flow past a smooth cylinder. The spectral power density for the flow calculated using URANS shows a dominant Strouhal number of 0.21, which is also in good agreement with measured data [13,48]. For cylinder 2, the mean drag coefficient is reduced moderately from the computed baseline turbulent value and significantly from the laminar value, which is approximately 1.0 [13]. The oscillations in lift and drag are completely suppressed for cylinder 2 due to spanwise-periodic porosity exciting a hydrodynamic convective instability.

## IX. Conclusions

Flow control using periodic porosity on the surface of a cylinder in a crossflow is studied. Experimental and numerical results complement each other and demonstrate the overall flow development. A periodic porous pattern is found to be significantly more effective than a uniform porous pattern in controlling separation. Although porosity is used in the present study, the fluid mechanism suggests that other forms of separation control can potentially provide similar effects. The results can be summarized as follows.

1. Experiments show that at a Reynolds number of $19 \times 10^3$, periodic porosity induces the formation of a series of steady counter-rotating structures behind the porous patches with or without suction being applied. A closing of the wake occurs when porosity is placed on both the top and bottom surfaces.

2. A similar phenomenon is observed in the numerical results with suction and assumed turbulent flow. The drag is reduced compared with both laminar and turbulent flows over a smooth cylinder.

3. Numerical results show that the formation of stable counter-rotating vortices downstream of each porous patch suppresses spanwise vortex shedding and the associated oscillation in lift. This conclusion is supported by hot-wire results that show a significant reduction in the velocity fluctuation level in the wake of the porous cylinder, compared with the solid cylinder.

4. Steady- and unsteady-state simulations fail to show, even at very high suction rates, sustained streamwise vortices when a laminar flow is assumed. Although many potential reasons exist, we suspect one of the main causes is the inability of the numerical scheme to accurately simulate a transition/separation point, the location of which affects the amplification of the instability responsible for the streamwise vortex formation.

5. Transient simulations (URANS) for the natural transpiration case did not successfully capture the experimental observed sustained streamwise vortices, regardless of the assumed state of the boundary layer. This could be due to low amplification rates of the instability for the natural transpiration case. Resolving this low amplification rate might require DNS.

## Acknowledgment

The authors thank Ohio Supercomputer Center for providing the required computational resources.

## References

[1] Ng, T. T., and Lang, Y., "Shear Layer Instability Induced Separation Control," *AIAA Journal*, Vol. 37, No. 3, 1999, pp. 386–388. doi:10.2514/2.721

[2] Lopera, J., and Ng, T. T., "Experimental Investigations of Reconfigurable Porosity for Aerodynamic Control," AIAA 2nd Flow Control Conference, AIAA Paper 2004-2695, 2004.

[3] Patel, M. P., DiCocco, J. M., Lopera, J., and Ng, T. T., "Active Boattailing and Aerodynamic Control Fins for Maneuvering Missiles," AIAA 2nd Flow Control Conference, AIAA Paper 2004-2696, 2004.

[4] Raghunathan, S., "Passive Control of Shock–Boundary Layer Interaction," *Progress in Aerospace Sciences*, Vol. 25, No. 3, 1988, pp. 271–296. doi:10.1016/0376-0421(88)90002-4

[5] Nagamatsu, H. T., Trilling, T. W., and Bossard, J. A., "Passive Drag Reduction on a Complete NACA 0012 Airfoil at Transonic Mach Numbers," AIAA Paper 1987-1263, 1987.

[6] Bauer, S. X. S., and Hernandez, G., "Reduction of Cross-Flow Shock-Induced Separation with a Porous Cavity at Supersonic Speeds," AIAA Paper 1988-2567, 1988.

[7] Raghunathan, S., "Passive Shockwave Boundary Layer Control Experiments on a Circular Arc Model," AIAA Paper 1986-0285, 1986.

[8] Nagamatsu, H. T., Brower, W. B., Bahi, L., and Marble, S. K., "Investigation of Passive Shock Wave/Boundary Layer Control for Transonic Airfoil Drag Reduction," NASA First Annual Report for Grant NSG1624, 1979.

[9] Wood, R. M., Banks, D. W., and Bauer, S. X. S., "Assessment of Passive Porosity with Free and Fixed Separation on a Tangent Ogive Forebody," AIAA Paper 1992-4494, 1992.

[10] Wilcox, F. J., "Experimental Investigation of the Effects of a Porous Floor on Cavity Flowfields at Supersonic Speeds," NASA TP 3032, 1990.

[11] Bauer, S. X. S., and Hemsch, M. J., "Alleviation of Sideforce on Tangent-Ogive Forebodies Using Passive Porosity," *Journal of Aircraft*, Vol. 31, No. 2, 1994, pp. 354–361. doi:10.2514/3.46494

[12] Hunter, C. A., Viken, S. A., Wood, R. M., and Bauer, S. X. S., "Advanced Aerodynamic Design of Passive Porosity Control Effectors," AIAA Paper 2001-0249, 2001.

[13] Zdravkovich, M. M., *Flow Around Circular Cylinders*, , Vol. 1: Fundamentals, Oxford Univ. Press, Oxford, 1997.

[14] Zdravkovich, M. M., *Flow Around Circular Cylinders*, Vol. 2: Applications, Oxford Univ. Press, Oxford, 2003.

[15] Oengoren, A., and Rockwell, D., "Flow Structure From an Oscillating Cylinder. Part 1: Mechanisms of Phase Shift and Recovery of the Near-Wake," *Journal of Fluid Mechanics*, Vol. 191, No. 1, 1988, pp. 197–223. doi:10.1017/S0022112088001569

[16] Nakano, M., and Rockwell, D., "Destabilization of the Karman Vortex Street by Frequency-Modulated Excitation," *Physics of Fluids A: Fluid Dynamics*, Vol. 3, No. 5, 1991, pp. 723–725. doi:10.1063/1.858004

[17] Choi, S., Choi, H., and Kang, S., "Characteristics of Flow over a Rotationally Oscillating Cylinder at Low Reynolds Number," *Physics of Fluids*, Vol. 14, No. 8, 2002, pp. 2767–2777. doi:10.1063/1.1491251

[18] Baek, S. J., Lee, S. B., and Sung, H. J., "Response of a Circular Wake to Super Harmonic Excitation," *Journal of Fluid Mechanics*, Vol. 442, No. 1, 2001, pp. 67–88.doi:10.1017/S0022112001004980

[19] Minn, C., and Choi, H., "Suboptimal Feedback Control of Vortex Shedding at Low Reynolds Numbers," *Journal of Fluid Mechanics*, Vol. 401, No. 1, 1999, pp. 123–156. doi:10.1017/S002211209900659X

[20] Konak, S., and Rockwell, D., "Control of the Spanwise Structure of a Bluff-Body Wake by Changes in the Boundary-Layer Thickness at Separation," *Physics of Fluids A: Fluid Dynamics*, Vol. 5, No. 2, 1993, pp. 509–511. doi:10.1063/1.858876

[21] Hammond, D. A., and Redekopp, L. G., "Global Dynamics and Aerodynamic Flow Vectoring of Wakes," *Journal of Fluid Mechanics*, Vol. 338, No. 1, 1997, pp. 231–248. doi:10.1017/S0022112096004818

[22] Hannemann, K., and Oertel, H., "Numerical Simulation of the Absolutely and Convectively Unstable Wake," *Journal of Fluid Mechanics*, Vol. 199, No. 1, 1989, pp. 55–88. doi:10.1017/S0022112089000297

[23] Leu, T. S., and Ho, C. M., "Control of Global Instability in a Non-Parallel Near Wake," *Journal of Fluid Mechanics*, Vol. 404, No. 1, 2000, pp. 345–378. doi:10.1017/S0022112099007272

[24] Arcas, D. R., and Redekopp, L. G., "Aspects of Wake Vortex Control Through Base Blowing/Suction," *Physics of Fluids*, Vol. 16, No. 2, 2004, pp. 452–456. doi:10.1063/1.1637354

[25] Macmanus, D. G., and Eaton, J. A., "Flow Physics of Discrete Boundary Layer Suction: Measurements and Predictions," *Journal of Fluid Mechanics*, Vol. 417, No. 1, 2000, pp. 47–75. doi:10.1017/S0022112000001026

[26] Roberts, P. J. D., and Floryan, J. M., "Boundary Layer Instability Induced by Surface Suction," *Physics of Fluids*, Vol. 13, No. 9, 2001, pp. 2543–2552. doi:10.1063/1.1384868

[27] Fransson, J. H. M., and Alfredsson, P. H., "On the Disturbance Growth in an Asymptotic Suction Boundary Layer," *Journal of Fluid Mechanics*, Vol. 482, No. 1, 2003, pp. 51–90. doi:10.1017/S0022112003003926

[28] Bakchinov, A. A., Westin, K. J. A., Kozlov, V. V., and Alfredsson, P. H., "Experiments on Localized Disturbances in a Flat Plate Boundary Layer, Part 2: Interaction Between Localized Disturbances and TS-Waves," *European Journal of Mechanics, B: Fluids*, Vol. 17, No. 6, 1998, pp. 847–873. doi:10.1016/S0997-7546(99)80017-X

[29] Launder, B. E., "Second-Moment Closure: Present... and Future?," *International Journal of Heat and Fluid Flow*, Vol. 10, No. 4, 1989, pp. 282–300. doi:10.1016/0142-727X(89)90017-9

[30] Launder, B. E., Reece, G. J., and Rodi, W., "Progress in the Development of a Reynolds-Stress Turbulence Closure," *Journal of Fluid Mechanics*, Vol. 68, No. 3, 1975, pp. 537–566. doi:10.1017/S0022112075001814

[31] Donovan, J. F., Kral, J. D., and Cary, A. W., "Active Flow Control Applied to an Airfoil," AIAA Paper 98-0210, 1998.

[32] Ravindran, S. S., "Active Control of Flow Separation Over an Airfoil," NASA TM 209838, 1999.

[33] Wu, J. Z., Lu, X.-Y., Denny, A. G., Fan, M., and Wu, J.-M., "Post-Stall Flow Control on an Airfoil by Local Unsteady Forcing," *Journal of Fluid Mechanics*, Vol. 371, No. 1, 1998, pp. 21–58. doi:10.1017/S0022112098002055

[34] Dejoan, A., Jang, Y.-J., and Leschziner, M. A., "Comparative LES and Unsteady RANS Computations for Periodically-Perturbed Separated Flow Over a Backward-Facing Step," *Journal of Fluids Engineering*, Vol. 127, No. 5, 2005, pp. 872–878. doi:10.1115/1.2033012

[35] Viken, S. A., Vatsa, V. N., Rumsey, C. L., and Carpenter, M. H., "Flow Control Analysis on the Hump Model with RANS Tools," AIAA Paper 2003-0218, 2003.

[36] Lubcke, H., Schmidt, S., Rung, T., and Thiele, F., "Comparison of LES and RANS in Bluff-Body Flows," *Journal of Wind Engineering and Industrial Aerodynamics*, Vol. 89, No. 14–15, 2001, pp. 1471–1485. doi:10.1016/S0167-6105(01)00134-9

[37] Rodi, W., "Comparison of LES and RANS Calculations of the Flow Around Bluff Bodies," *Journal of Wind Engineering and Industrial Aerodynamics*, Vol. 69–71, July–Oct. 1997, pp. 55–75. doi:10.1016/S0167-6105(97)00147-5

[38] Iaccarino, G., Ooi, A., Durbin, P. A., and Behnia, M., "Reynolds Averaged Simulation of Unsteady Separated Flow," *International Journal of Heat and Fluid Flow*, Vol. 24, No. 2, 2003, pp. 147–156. doi:10.1016/S0142-727X(02)00210-2

[39] Merigaud, E., "Structure of Turbulent Boundary Layer with Localized Wall Suction," Ph.D. Dissertation, Aix-Marseille II, Marseille, France, 1995.

[40] Djenidi, L., and Antonia, R. A., "Calculation of the Effect of Concentrated Wall Suction on a Turbulent Boundary Layer Using a

Second-Order Moment Closure," *International Journal of Heat and Fluid Flow*, Vol. 22, No. 5, 2001, pp. 487–494.
doi:10.1016/S0142-727X(01)00114-X

[41] Kim, S. E., "Large Eddy Simulation of Turbulent Flow Past a Circular Cylinder in Sub Critical Regime," AIAA Paper 2006-1418, 2006.

[42] Ng, T. T., "Control of Flow Separation Behind a Cylinder Using Discrete Suction," *AIAA Journal*, Vol. 39, No. 2, 2001, pp. 355–357.
doi:10.2514/2.1314

[43] Chyu, C.-K., and Rockwell, D., "Near Wake Flow Structure of a Cylinder with a Helical Surface Perturbation," *Journal of Fluids and Structures*, Vol. 16, No. 2, pp. 263–269.
doi:10.1006/jfls.2001.0419

[44] Lam, K., Wang, F. H., and So, R. M. C., "Three-Dimensional Nature of Vortices in the Near Wake of a Wavy Cylinder," *Journal of Fluids and Structures*, Vol. 19, No. 6, 2004, pp. 815–833.
doi:10.1016/j.jfluidstructs.2004.04.004

[45] Zhang, W., Daichin, and Lee, S. J., "PIV Measurements of the Near-Wake Behind a Sinusoidal Cylinder," *Experiments in Fluids*, Vol. 38, No. 6, 2005, pp. 824–832.
doi:10.1007/s00348-005-0981-9

[46] Lasheras, J. C., Cho, J. S., and Maxworthy, T., "On the Origin and Evolution of Streamwise Vortical Structures in a Plane, Free Shear Layer," *Journal of Fluid Mechanics*, Vol. 172, No. 1, 1986, pp. 231–258.
doi:10.1017/S0022112086001726

[47] Pierrehumber, R. T., and Widnall, S. E., "The Two- and Three-Dimensional Instabilities of a Spatially Periodic Shear Layer," *Journal of Fluid Mechanics*, Vol. 114, No. 1, 1982, pp. 59–82.
doi:10.1017/S0022112082000044

[48] Fey, U., Konig, M., and Eckelmann, H., "A New Strouhal–Reynolds-Number Relationship for the Circular Cylinder in the Range $47 < Re < 23 \times 10^5$," *Physics of Fluids*, Vol. 10, No. 7, 1998, pp. 1547–1549.
doi:10.1063/1.869675

F. Coton
*Associate Editor*